

Coseismic displacement estimate of the 2013 $M_S7.0$ Lushan, China earthquake based on the simulation of near-fault displacement field

Hong Zhou

Received: 2 August 2016 / Accepted: 27 September 2016 / Published online: 19 November 2016
© The Author(s) 2016. This article is published with open access at Springerlink.com

Abstract Usually, GPS observation provides direct evidence to estimate coseismic displacement. However, GPS stations are scattered, sparse and cannot provide a detailed distribution of coseismic displacement. Strong ground motion records share the same disadvantages as GPS in estimating coseismic displacement. Estimations from InSAR data can provide displacement distributions; however, the resolution of such methods is limited by the analysis techniques. The paper focuses on estimating the coseismic displacement of the $M_S7.0$ Lushan earthquake on April 20, 2013 using a simulation of the wave field based on the elastic wave equation instead of a quasi-static equation. First, the media and source models were constructed by comparing the simulated velocity and the record velocity of the ground motion. Then simulated static displacements were compared with GPS records. Their agreement validates our results. Careful analysis of the distribution of simulated coseismic displacements near the fault reveals more details of the ground motion. For example, an uplift appears on the hanging wall of the fault, rotation is associated with the horizontal displacement, the fault strike and earthquake epicenter provide the main control on motion near the faults, and the motion on the hanging wall is stronger than that on the footwall. These results reveal additional characteristics of the ground motion of the Lushan earthquake.

Keywords Lushan earthquake · Coseismic displacement · Simulation of the wave field · Spectral element method

H. Zhou (✉)
Institute of Geophysics, China Earthquake Administration,
Beijing 100081, China
e-mail: zhouhong@cea-igp.ac.cn

1 Introduction

At 08:02 on April 20, 2013 (Beijing time), a $M_S7.0$ earthquake (the moment magnitude calculated by the USGS was $M_W6.6$) took place in Lushan County, near the city of Yaan in Sichuan Province, China. This earthquake is a typical blind reverse-fault earthquake and the Shuangshi-Dachuan fault of the southern segment of the Longmenshan thrust belt may be its seismogenic fault (Xu et al. 2013). Many seismologists have done much works concerning its mechanisms, e.g., source rupture process inversion using teleseismic data (Hao et al. 2013; Zhang et al. 2013b, 2014; Wang et al. 2013; Liu et al. 2013), source inversion using GPS data (Jiang et al. 2014), the analysis of GPS and seismic data near the fault (Wu et al. 2013; Jiang et al. 2013; Du et al. 2013), seismic moment tensor inversion (Lin et al. 2013), the relocation of aftershocks (Han et al. 2014; Su et al. 2013; Zhao et al. 2013; Fang et al. 2013; Zhang et al. 2013c), and strong ground motion analysis associated with acceleration record (Xie et al. 2014; Wen and Ren 2014; Mooney and Wang 2014).

Usually, spatial distribution of coseismic displacements denotes the deformation of ground surface due to an earthquake. It represents a contribution of an earthquake to the change of landforms, which may be due to local non-elastic effects or elastic deformation caused by a fault. Accurate estimates of the coseismic displacement are a worthy goal. Nowadays, there are many methods being applied to such research. The use of GPS observations is the most common and direct method (Gu et al. 2009; Jiang et al. 2013; Wu et al. 2013). However, estimates made with this method are affected by the limited number of observational stations. Coseismic displacements deduced from GPS observation are scattered and sparse, thus the details of the ground motion near the fault are not well resolved.

Near-fault strong ground motion records provide another method for examining this coseismic displacement (Jin and Wang 2013; Jin et al. 2014; Chen and Loh 2007; Hu et al. 2007; Rupakhety et al. 2010; Jafarzadeh et al. 2009). In addition to the disadvantage of limited observation stations, such estimates are also affected by the correction method required by strong motion records; expert judgment is needed to assess the reasonability of each estimate (Peng et al. 2011). Satellite remote sensing images can also be used for coseismic displacement estimates (Zhang et al. 2007; Xu et al. 2014; Wan et al. 2008) though the resolution is limited. The reasonable simulation of the displacement field near the fault can provide a detailed distribution of coseismic displacement. Not only it provides overall distribution information, but also its resolution is high as well. Therefore, this study prefers to use the simulation of the wave field for estimating the distribution of coseismic displacement.

A quasi-static elastic wave equation, which omits the acceleration, is often applied for simulations of coseismic displacement. In fact, coseismic displacement is not a kind of independent displacement field, rather it is the final result of the development of the ground motion displacement. Therefore, I suggest that a simulation of dynamic displacement can provide more accurate information on coseismic displacement. This paper uses the elastic wave equation directly and applies the spectral element numerical method to simulate the displacement field of the Lushan earthquake due to source rupture process. The coseismic displacement is estimated by the permanent value of the displacements. Prior to the displacement simulation, the simulated ground velocities were compared with the velocities from strong ground motion records. Their agreements confirm the reasonability of the source and media model. Furthermore, the comparisons between the simulated results and coseismic displacements deduced from GPS validate our estimates. In Sect. 5, the distributions of coseismic displacement are analyzed and discussed, highlighting some interesting and significant phenomena concerning the ground motion observed in this region.

2 Simulation method

The spectral element method (Komatitsch and Vilotte 1998; Komatitsch and Tromp 2002; Komatitsch et al. 2004) was applied in the simulation. The underground propagation in a given medium is described by the wave equation with boundary and initial conditions that can be written as

$$\begin{aligned}\rho \mathbf{u} &= \nabla \cdot \boldsymbol{\sigma} + \mathbf{f} \\ \boldsymbol{\sigma} &= \mathbf{C} : \boldsymbol{\varepsilon} \\ \boldsymbol{\varepsilon} &= \frac{1}{2} [\nabla \mathbf{u} + (\nabla \mathbf{u})^T],\end{aligned}\quad (1)$$

where \mathbf{u} is the displacement vector, $\boldsymbol{\sigma}$ is the stress tensor, \mathbf{C} is the stiffness tensor, ρ is the density, \mathbf{f} is the external force, and T denotes transposition. The colon symbol in the equation denotes multiplication by a tensor and the dots above the \mathbf{u} denote a time derivative.

For the above equation, an arbitrary test function, \mathbf{w} , is multiplied on both sides. Using integration by parts, Eq. (2) is obtained as follows:

$$\begin{aligned}\int_{\Omega} \rho \mathbf{w} \cdot \mathbf{u} d\Omega + \int_{\Omega} \nabla \mathbf{w} : \mathbf{C} : \nabla \mathbf{u} d\Omega &= \int_{\Omega} \mathbf{w} \cdot \mathbf{f} d\Omega \\ + \int_{\Gamma} \mathbf{w} \cdot \mathbf{t} d\Gamma,\end{aligned}\quad (2)$$

where Ω is the computation zone, Γ is the boundary that includes the free surface and the artificial boundary, and \mathbf{t} is the traction on Γ .

For the spectral element method (SEM), the area to be calculated is first divided into non-overlapping discrete small elements with six surfaces. The Gauss-Lobatto-Legendre (GLL) points are computed for each element. Finally, denoting the global vector of unknown displacement by \mathbf{U} , the matrix equation of Eq. (2) was obtained as follows:

$$\mathbf{M}\mathbf{U} + \mathbf{K}\mathbf{U} = \mathbf{F},\quad (3)$$

where \mathbf{M} is the mass matrix, \mathbf{K} is the stiffness matrix, and \mathbf{F} is the source term. In this procedure, the application of GLL points in conjunction with the GLL integration rule renders the mass matrix \mathbf{M} exactly diagonal, thereby resulting in drastic reductions in computational cost of the algorithm. This is a major advantage of the SEM. In the following simulation, the time interval is set as 0.01 s and the small elements are set as 2 km. In each direction of small elements, 7 GLL points are applied.

3 Source and media models

Figure 1 shows the region of latitude 29.5°N–31.5°N and longitude 102°E–104°E. In the figure, the study area is indicated by a yellow square having sides of 110 km. The media parameters applied in our simulation were constructed by an interpolation of the crust1.0 model with the topography. Figure 2 shows the varying V_p along the profile AB shown in Fig. 1. Obviously, the model used in computation is 3D irregular layer media. The rupture process of the Lushan earthquake has been investigated by

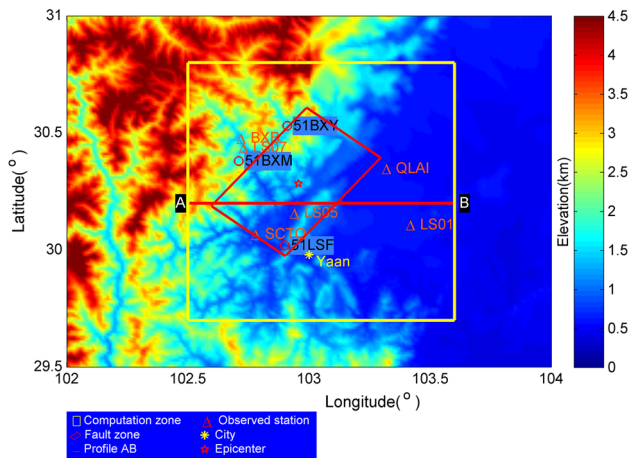


Fig. 1 Simulation region and observed stations

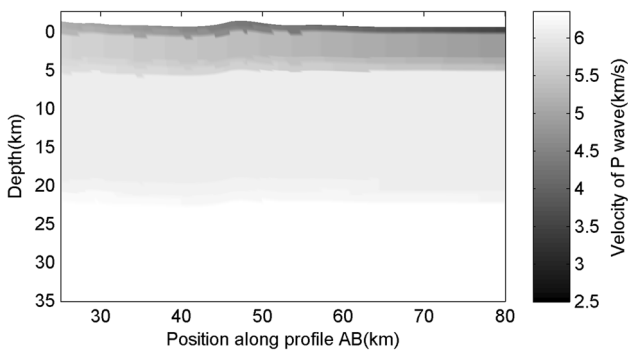


Fig. 2 Velocity structure of P wave under the profile AB

many inversion works. On the whole, the results of these inversions are similar; however, their differences are not trivial (Hao et al. 2013; Zhang et al. 2013a, 2014; Wang et al. 2013; Liu et al. 2013; Jiang et al. 2014). Zhang et al. (2013b, 2014) provided not only the slip distribution but also the slip-rate time function on the faults. I simulated ground motion using the sources inverted by Zhang et al. (2013b) and Zhang et al. (2014) and compared them with observed records respectively and found those of Zhang et al. (2013b) providing a closer agreement for the media model used in this study. So their result (Zhang et al. 2013b) was applied as the source function in this study. The details of the source can be found in Zhang et al. (2013b). The left panel of Fig. 3 shows the slip distribution on the fault and the right panel displays the slip-rate time function along the strike across epicenter.

4 Comparisons of simulated results with strong ground motion records

In Fig. 1, near the fault there are three observed stations of strong ground motion denoted by red open circles and six

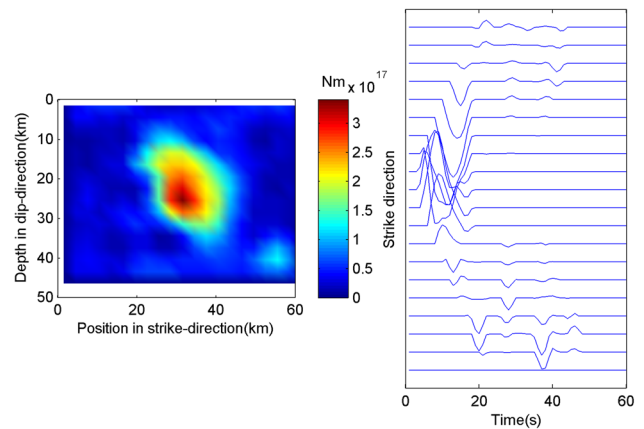


Fig. 3 Left panel the earthquake moment distribution on the fault surface. Right panel the slip rate along strike across the epicenter

GPS stations denoted by red triangles. The epicenter is denoted by the red star and the red box is the projection of the fault plane on the ground surface. The left column in Fig. 4 shows the acceleration records in three directions at stations 51BXY, 51BXM, and 51LSF. Obviously, they contain abundant high-frequency information. Due to the low frequency of the source (less than 0.1 Hz) and the limitation of computation technique and computation equipment, only the acceleration in low-frequency band can be simulated. Thus, the low-frequency simulation results and acceleration records need to be filtered by the same low-pass filter for comparison. The middle column in Fig. 4 shows the comparison between the simulation results and the acceleration records filtered by the same low-pass filter. The right column shows the comparison between the simulation velocities and the recorded velocities which were also filtered by the same low-pass filter. Comparisons of the 18 records at three stations show that both velocity and acceleration simulation results have waveforms and values similar to those of the observed records. For instance, both have a large trough and peak with similar periods. These agreements illustrate that the source used can represent the actual main rupture of the $M_S7.0$ earthquake and that the wave propagation in the model can reflect the main wave information at low frequencies. Thus, the estimation of coseismic displacement with lower frequencies based on the same source and media model can be considered trustworthy.

Usually, the displacement has a lower frequency than the velocity. Figure 5 shows the simulated displacements at stations 51BXY, 51BXM, and 51LSF. The unfiltered result is denoted by black lines and the filtered one is represented by a red line. Obviously, the displacements in all three directions have static displacements that can be considered as the actual permanent movement at the stations. To remove probable high frequencies in the static

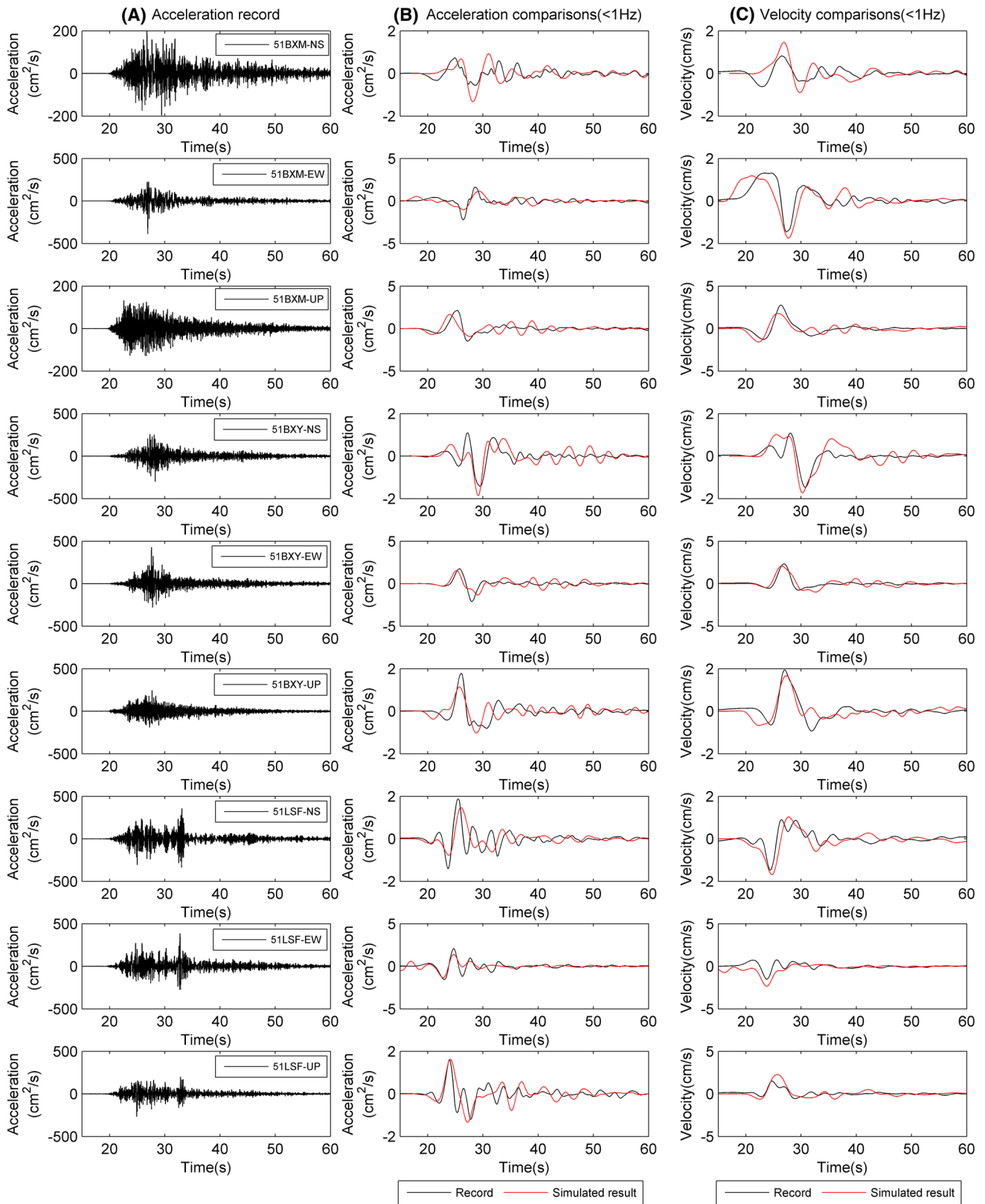


Fig. 4 Acceleration record in three directions at 51BXY, 51BXM, and 51LSF ground motion stations, and the comparison of velocity records and acceleration records with that of simulated results

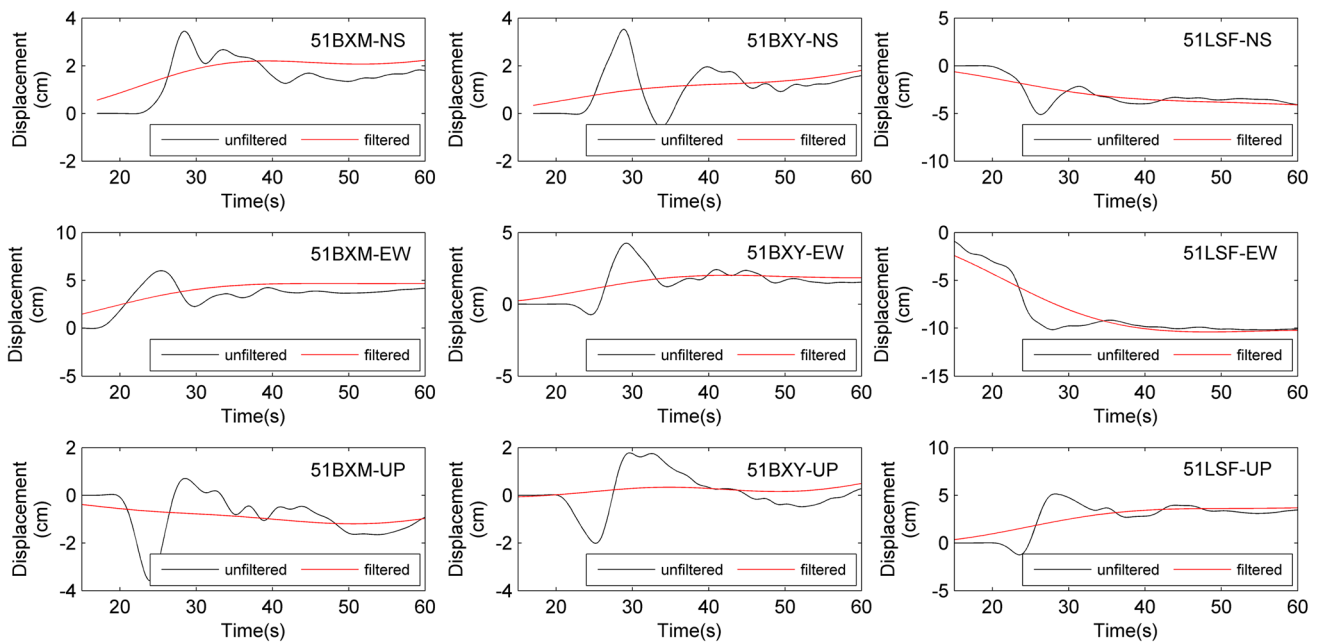


Fig. 5 Comparisons of the filtered and unfiltered simulated displacements at stations 51BXY, 51BXM, and 51LSF

displacement, we used the filtered value to estimate the coseismic displacement field of the Lushan earthquake.

Before analyzing the coseismic displacement field, a further evaluation of the simulated coseismic displacement needs to be undertaken by comparing GPS stations. We gathered GPS data from six stations within the computation domain. Their horizontal and vertical displacements, as compared with the simulated displacement at the corresponding locations, are shown in Table 1. The absolute difference (about 2 cm) of point LS05 is the largest. However, the difference is not large relative to GPS measurements of the point (8.75 cm). The simulated displacements at LS07 are mostly consistent with displacement records; their differences are less than the observed GPS errors. The difference in other measurements at points LS01, SCTQ, and BXB is less than 1 cm. The relative difference at station QLAI is the greatest, possibly because of its special position. The following Sect. 5 will show that

this station is located very close to the fault line *AB*, where very strong changes in ground motion occurred. Despite this, the relative difference at station QLAI is nearly equal to its relative measurement error of GPS. Therefore, the differences between the simulation results and GPS data are considered reasonable, and the simulation results can represent the actual coseismic displacement. Figure 6 shows the comparisons of horizontal displacement vectors at stations LS01, LS07, and BXB. Not only are their values similar, but also their directions of motion agree to each other. The vector comparisons on the other three stations are not as good as those on the three stations LS01, LS07, and BXB, so their comparisons are omitted. In Figs. 7, 8, 9, and 10, there is a starting (*) point at 30.20°N, 102.94°E, which has an upward moving displacement of 19.843 cm from level measurement (Hao et al. 2014), whereas the corresponding simulation result is about 20 cm. Their difference is, thus, less than 2 mm. The comparisons above

Table 1 Comparisons between the simulated results and coseismic displacement determined by GPS

Station	Longitude	Latitude	Vertical displacement (cm)			Horizontal displacement (cm)		
			Simulation	GPS	Difference	Simulation	GPS	Difference
LS01	103.38°	30.11°	0.83	0.03 ± 0.32	0.48	1.50	1.77 ± 0.10	0.10
LS05	102.92°	30.16°	10.40	8.36 ± 0.37	1.67	8.97	6.75 ± 0.18	2.04
LS07	102.71°	30.44°	-0.48	-0.46 ± 0.61	0.0	2.94	2.99 ± 0.15	0.00
QLAI	103.30°	30.35°	0.44	-0.49 ± 0.41	0.53	2.08	1.16 ± 0.11	1.31
SCTQ	102.76°	30.07°	0.40	0.58 ± 0.48	0	2.95	2.11 ± 0.14	0.70
BXB	102.70°	30.48°	-0.44	-0.67	0.23	3.81	4.41	0.60

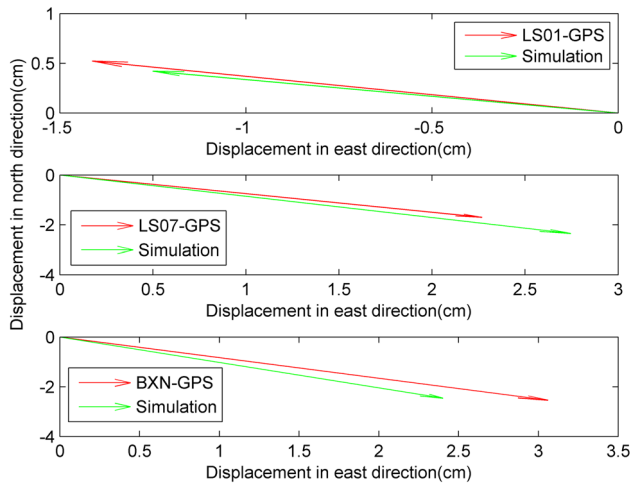


Fig. 6 Comparison of *horizontal* vector motions at the three GPS stations and the simulated results

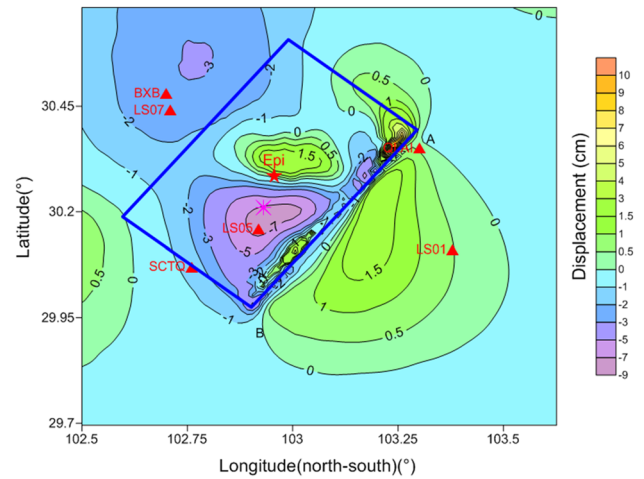


Fig. 8 Distribution of north-south-oriented coseismic displacement. The *blue box* denotes the projected zone of the fault surface on the ground, the *triangles* denote station

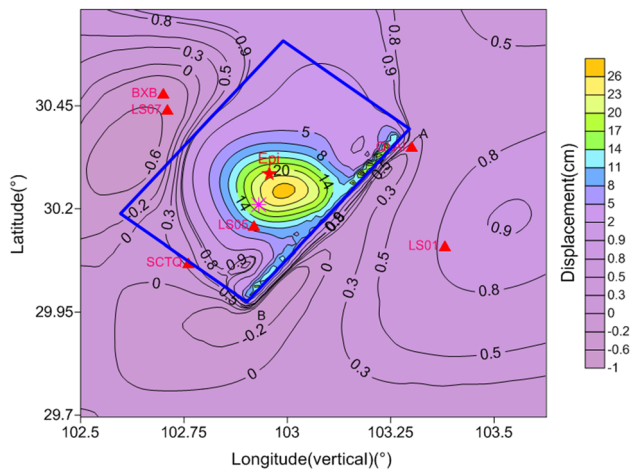


Fig. 7 Distribution of *vertical* coseismic displacements. *Asterisk* indicates the level measurement point. The *blue box* denotes the projected zone of the fault surface on the ground, the *triangles* denote station

prove that our estimates of coseismic displacement indeed represent actual ground motions.

5 Coseismic displacement distribution analysis

Figures 7, 8, 9, and 10 show the distribution of the coseismic displacements obtained from the static displacement of simulated wave propagation. To conveniently describe displacements, we introduce two concepts: one is the projection region that corresponds to the projected zone of the fault surface on the ground as denoted by a blue box in Figs. 7, 8, 9, and 10; the other is the fault line *AB* (Figs. 7, 8, 9, 10) corresponding to the fault trace on the surface. The star symbol indicates the epicenter.

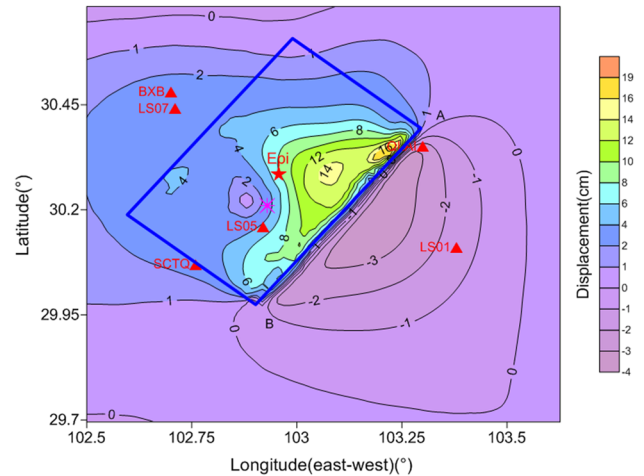


Fig. 9 Distribution of east-west-oriented coseismic displacement. The *blue box* denotes the projected zone of the fault surface on the ground, the *triangles* denote station

Figure 7 illustrates the distribution of vertical displacement. An uplift is obvious in the vicinity of the epicenter, where upward motion is more than 25 cm. The uplift spreads in a circular pattern as indicated by 5-cm interval contour lines with a radius <25 km. The appearance of the uplift agrees to the assumption of Chen et al. (2014) who showed that there should be an uplift zone on the hanging wall. In the northwest, away from the projection region, there is a zone of depression with a decrease in elevation of <1 cm. This region is produced by the uplift motion. Along the fault line *AB*, there are small areas distributed like beads with large upward motion that exceeds 20 cm, and near the south end of *AB*, there is also a weak depressed zone with upward motion around it. Repeatedly, near the epicenter in this figure there is a star point (30.2°N,

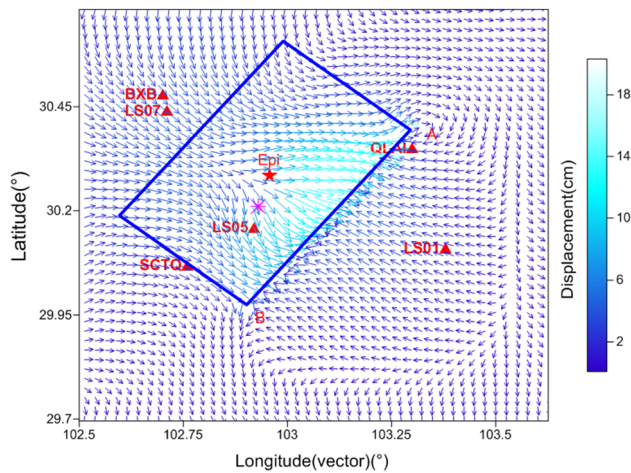


Fig. 10 Distribution of *horizontal* vectors of coseismic displacement. The *blue box* denotes the projected zone of the fault surface on the ground

102.94°E) with an upward motion of 19.843 cm (Hao et al. 2014), matching our simulated value of 20 cm. This similarity shows the reliability of our result. In comparison with the hanging wall, the motion on the footwall is simple with a rising displacement less than 1 cm. On the whole, the uplift near the epicenter is dominant that controls the vertical motion near the fault.

The distribution of motions in the north-south direction is shown in Fig. 8. It is clear that the movement on the hanging wall can be divided into three parts: outside the projection area, southward motion dominates with displacement less than 3 cm; within the projection area, motion in the southern part is toward the south with displacement more than 7 cm, while in the northern part it is toward the north and less than 2 cm. These opposite motions result from uplift near the epicenter. The rising ground pushes the material adjacent to the epicenter to the north and south. Note that along the fault line *AB* motions are very complex. The northward and southward motions appear alternatively. This alternating motion is apparently determined by the alternative rise and fall along the fault line *AB*. In the northern section of the line, the maximum motion to the north exceeds 8 cm. The northward motion near the left boundary of the simulation zone may be explained by the downward-oriented motion near this area. Of course, the amplitude of this motion is small and is only a subordinate motion. On the footwall, the northward-oriented motion only occurs in a half circle near the fault with a value less than 2 cm.

Figure 9 shows the contours of east-west-oriented motion. On the whole, motion on the hanging wall is >0 cm, indicating move to the east, whereas on the footwall the value is <0 cm, denoting move to the west. The distribution also shows that in the fault projection area the

movement is complex, as demonstrated by a strong variation of the contours. In the northeastern part of the projection, there are two strong movement zones: one lies just to the east of the epicenter with the largest motion exceeding 14 cm, and the other appears near the northern section of fault line *AB* and exceeds 16 cm. Near the center of the projection, there is a small zone where the motion in the west-east direction is close to zero; this region lies near the epicenter and has an area of about 3.0 km \times 3.0 km. In contrast to the hanging wall, the footwall shows not only low level of motion (with magnitudes <3 cm), but also a weak change of motion.

To illustrate the horizontal motion more clearly, vector horizontal displacements are shown in Fig. 10. This illustrates very interesting movements. On the hanging wall, the epicenter and fault line *AB* control the distribution of ground motion. Outside the projection area, the ground moves toward the projection. In the center of the projection, the epicenter controls the motion. Although the epicenter itself has little horizontal displacement, it forces the surrounding zone to move toward the northeast, east, and southeast as the epicentral distances increase. When these motions intersect the fault line, they stop or change direction. Therefore, in the northern section of fault line *AB*, the motion becomes strike slip, whereas in the middle section it is perpendicular to *AB* and in the southern section it is oblique to *AB*. Differently on the footwall, within 40 km from the fault line, the slight movements are toward the northwest. Furthermore, in the northeast and southwest parts of the fault projection, there appear to be some rotational motions, such as eastward motions turning toward southeastward and then southward. On the whole, the southeastward motion is the main horizontal movement observed. From the above analysis, we can see that southeastward and upward motion dominates in the area, whereas the northward movement is driven by upward motions.

6 Conclusions

The paper simulated the wave field near the fault that hosted the $M_S7.0$ Lushan earthquake using the spectral element method. The inverted rupture process has been applied as the source. The media model was constructed based on the parameters of the *crust1.0* model. First, the simulated ground velocity was compared with the ground motion records that were filtered to a low-frequency band. The agreement in this comparison proves that the media and source applied in the computation can provide a reasonable simulation for the low-frequency band. Therefore, the static displacement in the simulated wave field can be used to estimate coseismic displacement. The estimated

coseismic displacements were then compared with the corresponding GPS data. These comparisons indicate that the displacements in horizontal or vertical direction are similar. In Sect. 5, we carefully analyzed the distribution of simulated coseismic displacement and found that the distribution suggests the following characteristics.

- (1) The motion on the hanging wall is greater than that on the footwall.
- (2) For vertical motion, the greatest displacement (>20 cm) occurs close to the epicenter on the hanging wall, manifesting as an uplifted zone. Twenty-five kilometers away from this location, the vertical motion decreases rapidly to less than 5 cm.
- (3) On the hanging wall, east-west-oriented motion is all toward the east. The largest motion (about 16 cm) occurs in the northern section of the fault.
- (4) For south-north-oriented motion, there are two oppositely moving regions: one toward the north and the other toward the south. They are controlled by upward motion proximal to the epicenter.
- (5) The vector distribution of horizontal motion shows that the horizontal motion is complex. Rotational and along-strike movements all appear at different epicentral distances. In contrast to the hanging wall, motion on the footwall is simple with displacement <1 cm.

The above analysis shows that an estimation of coseismic displacement from a simulated wave field provides more information on ground motion for the Lushan earthquake. This is meaningful to help us understand the topography change resulting from a strong earthquake. However, the above descriptions only prove that the estimate is effective for the Lushan earthquake. Further study is needed to clarify whether this kind of estimation can be applied to other earthquakes or not. Besides, in Lushan earthquake there were lots of coseismic landslides; do the coseismic landslides affect the coseismic surface displacement? What relations are there between the coseismic landslides and the coseismic displacement? These scientific questions need to be answered in the future.

Acknowledgments We appreciate Dr. Yong Zhang for his provision of the inversion source. This study was supported by the Earthquake Public Welfare Scientific Research Special Project (No. 201408014).

Open Access This article is distributed under the terms of the Creative Commons Attribution 4.0 International License (<http://creativecommons.org/licenses/by/4.0/>), which permits unrestricted use, distribution, and reproduction in any medium, provided you give appropriate credit to the original author(s) and the source, provide a link to the Creative Commons license, and indicate if changes were made.

References

- Chen SM, Loh CH (2007) Estimating permanent ground displacement from near-fault strong-motion accelerograms. *Bull Seismol Soc Am* 97(1):63–75
- Chen LC, Wang H, Ran YK, Lei SX, Li X, Wu FY, Ma XQ, Liu CL, Han F (2014) The 2013 Lushan $M_S7.0$ Earthquake: varied seismogenic structure from the 2008 Wenchuan earthquake. *Seismol Res Lett* 85(1):34–39
- Du YJ, Wang ZM, Yang SJ, An JC, Liu Q, Che GW (2013) Co-seismic deformation derived from GPS observations during April 20th, 2013 Lushan earthquake, Sichuan, China. *Earthq Sci* 26(3–4):153–160
- Fang LH, Wu JP, Wang WL, Lu ZY, Wang CZ, Yang T, Cai Y (2013) Relocation of the mainshock and aftershock sequences of $M_S7.0$ Sichuan Lushan earthquake. *Chin Sci Bull* 58(28–29):3451–3459
- Gu GH, Wan G, Wu X (2009) Coseismic displacements from the 2008 Wenchuan $M8.0$ earthquake observed by GPS. *Earthquake* 29(1):92–99
- Han LB, Zeng XF, Jiang CS, Ni SD, Zhang HJ, Long F (2014) Focal mechanisms of the 2013 $M_W6.6$ Lushan China earthquake and high-resolution aftershock relocations. *Seismol Res Lett* 85:8–14
- Hao J, Ji C, Wang W, Yao Z (2013) Rupture history of the 2013 $M_W6.6$ Lushan earthquake constrained with local strong motion and teleseismic body and surface waves. *Geophys Res Lett* 40(20):5371–5376
- Hao M, Wang QL, Liu LW, Shi Q (2014) Interseismic and coseismic displacements of the Lushan $M_S7.0$ earthquake inferred from leveling measurements. *Chin Sci Bull* 59:5129–5135
- Hu JC, Cheng LW, Chen HY, Wu YM, Lee JC, Chen YG, Lin KC, Rau RJ, Hao KC, Chen HH, Yu SB, Angelier J (2007) Coseismic deformation revealed by inversion of strong motion and GPS data: the 2003 Chengkung earthquake in eastern Taiwan. *Geophys J Int* 169(2):667–674
- Jafarzadeh F, Khatam H, Jahromi HF (2009) Application of base-line correction methods to obtain permanent displacements of a near-source ground motion: the 2003 Bam earthquake. *J Earthq Eng* 13(3):313–327
- Jiang FY, Zhu LY, Zhang X, Wang SX, Ji LY (2013) Deformation preparation background of Lushan $M_S7.0$ earthquake and its coseismic response. *J Seismol Res* 36(4):450–454
- Jiang ZS, Wang M, Wang YZ, Wu YQ, Che S, Shen ZK, Bürgmann R, Sun JB, Yang YL, Liao H, Li Q (2014) GPS constrained coseismic source and slip distribution of the 2013 $M_W6.6$ Lushan, China, earthquake and its tectonic implications. *Geophys Res Lett* 41(2):407–413
- Jin MP, Wang RJ (2013) Rapid slip inversion using co-seismic displacement data derived from near-source strong motion records. *Chin J Geophys* 56(4):1207–1215 (**in Chinese with English abstract**)
- Jin MP, Wang RJ, Tu HW (2014) The slip model and coseismic displacement field derived from near-source strong motion records of the Lushan $M_S7.0$ earthquake on 20 April 2013. *Chin J Geophys* 57(1):129–137 (**in Chinese with English abstract**)
- Komatitsch D, Vilotte JP (1998) The spectral element method. An efficient tool to simulation the seismic response of 2D and 3D geological structure. *Bull Seismol Soc Am* 88:368–392
- Komatitsch D, Tromp J (2002) Spectral-element simulations of global seismic wave propagation—I. Validation. *Geophys J Int* 149(2):390–412
- Komatitsch D, Liu Q, Tromp J, Suss P, Stidham C, Shaw JH (2004) Simulations of ground motion in the Los Angeles Basin based upon the spectral-element method. *Bull Seismol Soc Am* 94:187–206

- Lin XD, Ge HK, Xu P, Dreger D, Su JR, Wang BS, Wu MJ (2013) Near field full wave inversion: Lushan magnitude 7.0 earthquake and its aftershock moment tensor. *Chin J Geophys* 56(12):4047 (**in Chinese with English abstract**)
- Liu CL, Zheng Y, Ge C, Xiong X, Hsu HT (2013) Rupture process of the $M_S7.0$ Lushan earthquake. *Sci China* 56:1187–1192
- Mooney WD, Wang HL (2014) Seismic intensities, PGA, and PGV for the 20 April 2013 $M_W6.6$ Lushan China earthquake and a comparison with North America. *Seismol Res Lett* 85:1034–1042
- Peng XB, Li XJ, Liu QF (2011) Advances and methods for the recovery of coseismic displacements from strong-motion accelerograms. *World Earthq Eng* 27(3):73–80
- Rupakhetty R, Halldorsson B, Sigbjörnsson R (2010) Estimating coseismic deformations from near source strong motion records: methods and case studies. *Bull Earthq Eng* 8(4):787–811
- Su JR, Zheng Y, Yang JS, Chen TC, Wu P (2013) Accurate location of the Lushan, Sichuan $M7.0$ earthquake on 20 April 2013 and its aftershocks and analysis of the seismogenic structure. *Chin J Geophys* 56(8):2636–2644 (**in Chinese with English abstract**)
- Wan YG, Shen ZK, Wang M, Zhang ZS, Gan WJ, Wang QL, Sheng SZ (2008) Coseismic slip distribution of the 2001 Kunlun mountain pass west earthquake constrained using GPS and InSAR data. *Chin J Geophys* 51(4):1074–1084 (**in Chinese with English abstract**)
- Wang WM, Hao JL, Yao ZX (2013) Preliminary result for rupture process of Apr. 20, 2013 Lushan earthquake, Sichuan, China. *Chin J Geophys* 56(4):1412–1417 (**in Chinese with English abstract**)
- Wen RZ, Ren YF (2014) Strong-motion observations of the Lushan earthquake on 20 April 2013. *Seismol Res Lett* 85:1043–1055
- Wu YQ, Jiang ZS, Wang M, Che S, Liao H, Li Q, Li P, Yang YL, Xiang HP, Shao ZG, Wang WX, Wei WX, Liu XX (2013) Preliminary results of the co-seismic displacement and pre-seismic strain accumulation of the Lushan $M_S7.0$ earthquake reflected by the GPS surveying. *Chin Sci Bull* 58:1910–1916
- Xie JJ, Li XJ, Wen ZP, Wu CQ (2014) Near-source vertical and horizontal strong ground motion from the 20 April 2013 $M_W6.8$ Lushan earthquake in China. *Seismol Res Lett* 85:23–33
- Xu XW, Wen XZ, Han ZJ, Chen GH, Li CY, Zheng WJ, Zhang SM, Ren ZQ, Xu C, Tan XB, Wei ZY, Wang MM, Ren JJ, He ZT, Liang MJ (2013) Lushan $M_S7.0$ earthquake: a blind reverse-fault event. *Chin Sci Bull* 58(28–29):3437–3443. doi:10.1007/s11434-013-5999-4
- Xu KK, Niu YF, Wu JC (2014) Establishment of 3D coseismic terrain displacement field with GPS and InSAR. *J Geod Geodyn* 34(1):15–23
- Zhang L, Wu J, Chen YL, Xiao F (2007) Determination of coseismic displacement of field of Taiwan Chi-Chi earthquake based on Doris. *J Geod Geodyn* 27(3):18–24
- Zhang QZ, Tang WQ, Liu YQ, Li J (2013a) Co-seismic displacement of the $M_S7.0$ Lushan earthquake based on GPS monitoring. *Earth Sci Front* 20(6):42–47
- Zhang Y, Xu LS, Chen YT (2013b) Rupture process of Rupture process of the Lushan 4.20 earthquake and preliminary analysis on the disaster-causing mechanism. *Chin J Geophys* 56(4):1408–1411 (**in Chinese with English abstract**)
- Zhang ZQ, Wang WT, Ren ZK, Zhang PZ, Fang LH, Wu JP (2013c) Coseismic deformation and rupture processes of the 2013 Lushan earthquake. *Chin Sci Bull* 58(28–29):3483–3490
- Zhang Y, Wang RJ, Chen YT, Xu LS, Du F, Jin MP, Tu HW, Dahm T (2014) Kinematic rupture model and hypocenter relocation of the 2013 $M_W6.6$ Lushan earthquake constrained by strong-motion and teleseismic data. *Seismol Res Lett* 85:15–22
- Zhao B, Gao Y, Huang ZB (2013) Double difference relocation, focal mechanism and stress inversion of Lushan $M_S7.0$ earthquake sequence. *Chin J Geophys* 56(10):3385–3395 (**in Chinese with English abstract**)